Characteristics of neutron emission profile from neutral beam heated plasmas of the Large Helical Device at various magnetic field strengths

Characteristics of Neutron Emission Profile from Neutral Beam Heated Plasmas of the Large Helical Device at Various Magnetic Field Strengths

K. Ogawa[1,2], M. Isobe[1,2], S. Sugiyama[3], D. A. Spong[4], S. Sangaroon[1,5], R. Seki[1,2], H. Nuga[1], H. Yamaguchi[1,2], S. Kamio[1], Y. Fujiwara[1], M. I. Kobayashi[1,2], J. Jo[6], and M. Osakabe[1,2]

[1]National Institute for Fusion Science, National Institutes of Natural Sciences

[2]The Graduate University for Advanced Studies, SOKENDAI

[3] National Institutes for Quantum and Radiological Science and Technology

[4]Oak Ridge National Laboratory

[5]Mahasarakham University

[6]Korea Institute of Fusion Energy

ogawa.kunihiro@nifs.ac.jp

Abstract

The neutron emission profile of deuterium plasma in the Large Helical Device was measured with a multi-sightline vertical neutron camera under various magnetic field strength conditions. It was found that the line-integrated neutron emission profile shifts outward in the co-neutral beam (NB) case and inward in the counter neutral beam case.

Here, co- and counter directions correspond to enhance and reduce the poloidal magnetic field directions, respectively. The shift becomes more significant when the magnetic field decreased in strength. The experimentally obtained neutron emission profile was compared with the orbit-following models simulated through the DELTA5D code. The calculated neutron emission profiles vary according to the magnetic field strength because of the change of beam ion orbit and the slowing down due to the plasma parameter changes. Although a relatively narrow profile was obtained in the calculations at the inboard side for the co-NB case in the relatively low field condition, the profiles obtained through calculation and experiment were almost qualitatively aligned.

1. Introduction

In a fusion reactor, neutrons are mainly created by deuterium-tritium fusion reactions. Because the neutron does not have an electrical charge, neutrons directly escape from the plasma without interacting with the magnetic field. The energy of neutrons absorbed by a blanket module will be used for generating electricity. Understanding of the fusion reaction profile through the measurement of the spatial profile of neutron emission is essential in controlling the output power from a fusion burning plasma. Understanding the fusion reaction profile in an existing fusion machine in various neutron

emission conditions can contribute to an understanding of a fusion reaction profile in a fusion reactor. Also, a fusion burning plasma is sustained by deuterium-tritium fusion-born energetic alpha particles [1]. Thus, in the interest of understanding energetic ion behavior in a fusion burning plasma, the study of energetic ion confinement in magnetic confinement fusion devices has received much attention. In present day devices neutrons are primarily created by beam-plasma reactions, as observed in many previous neutral beam (NB) injection experiments [2]. As such, in NB-heated plasma, neutron diagnostics are some of the most powerful tools for obtaining information on the fusion reaction and energetic particles confined in the plasma core region. In particular, neutron emission profile diagnostics are some of the most effective methods for understanding the spatial profile of fusion reaction and energetic particle density. Neutron cameras have been used to measure the time-dependent neutron emission profile in large tokamaks, in which the total neutron emission rate (S_n) is in an order of 10^{16} n/s [3-5]. Neutron cameras also provide an understanding of the radial profiles of energetic particles and the effect of magnetohydrodynamic instabilities on energetic particle transport [6].

Energetic particle studies are also performed in stellarator/helical devices which have an advantage in long time sustainment of plasma compared with tokamaks. Particle orbits are relatively more complicated than tokamaks because of the relatively complex

structure of winding coils and the poloidal cross-section of plasma changes according to the toroidal angle. Previously, studies of energetic particle confinement have been performed based on charge-exchanged energetic particle measurements [7, 8] and lost energetic ion measurements [9, 10] because experiments are performed in relatively small devices or hydrogen experiments where the discussion of the energetic particle confinement was pretty limited. The first deuterium experiment in which the expected S_n was on the order of 10^{16} n/s was initiated in the Large Helical Device (LHD) [11-14]. In helical systems, the measurement of the fusion reaction profile has become possible for the first time in LHD. Three sets of vertical neutron cameras were installed in the LHD to understand the energetic ion confinement in stellarators or helical systems [15-19]. In helical systems, experiments can be conducted in a relatively wide range of magnetic field and plasma parameter ranges because the magnetic surfaces are created primarily by external coils. Previous measurements of the neutron emission profile were mainly performed at a B_t of ~2.75 T, for which S_n is relatively high [10-25]. In this study, the neutron emission profile was investigated for various B_t to show the ability of the neutron emission profile measurement in a fusion plasma as well as in the interest of developing a more fundamental understanding of beam ion confinement. A preliminary result of neutron emission profile measurement in the co-NB injection case at a B_t of 1.375 T

revealed that the line-integrated neutron emission profile becomes broader for B_t of 1.375 T than B_t of 2.75 T [26]. This paper reports the measurement of neutron emission profiles from deuterium LHD plasma under various B_t conditions using co- and counter NB injections. Comparisons with orbit-following will also be provided.

2. Experimental Setups

The LHD has five intensive NB injectors (Fig. 1). Three NB injectors (N-NBs) with negative-ion sources inject NBs in the tangential direction. The typical acceleration energy and injection power in deuterium injection are ~180 keV and ~2 MW, respectively. Two N-NBs (NB1 and NB3) create counter-going transit beam ions, and one N-NB (NB2) creates co-going transit beam ions in the experiment, with the direction of the toroidal magnetic field being clockwise or counterclockwise when viewed from the top. The other two NB injectors (P-NBs) with positive-ion sources inject NBs in the perpendicular direction. S_n is measured by the calibrated fission chamber detector, which is part of the neutron flux monitor located on the top of LHD [27, 28]. The time evolution of S_n with 0.5 ms resolution can be obtained. Central electron temperature (T_{e0}) is measured by Thomson scattering diagnostics every 33 ms [29]. Line-averaged electron density (n_{e_avg}) is measured by a far-infrared interferometer [30]. The radial neutron profile is measured

by a vertical neutron camera 1 (VNC1), as shown in Figure 2 (a). The VNC1 characterized by higher spatial resolution measurement is composed of a multichannel collimator, eleven stilbene scintillation detectors, and a novel data acquisition system capable of operation with a MHz pulse rate range with simultaneous online and offline neutron and gamma-ray discrimination functions. Here, the online discrimination meant that the data acquisition system provides the pulse shape parameter for discriminating neutron and gamma-ray, whereas the offline discrimination meant that the data acquisition system provides signal waveforms for post pulse shape discrimination analysis. The inner diameter of each multichannel collimator and the stilbene scintillator diameter is 30 mm and 20 mm, respectively. The anode signal of the stilbene detector is directly fed into the data acquisition system, which is composed of a 50-ohm 1 GHz sampling analog-to-digital convertor and field-programmable gate arrays. The shield box made by stainless steel covers the signal cables from the scintillation detector to the analog-to-digital converter. Figure 2 (b) shows the sightlines of the VNC1 together with the magnetic flux surfaces at the magnetic axis position, R_{ax}, of 3.60 m at the installation position of the VNC1. The entire plasma region is covered with ten vertical chords. Note that the outermost vertical chord is for measuring background-scattering neutrons.

3. Experimental Results

3.1 Measurement of neutron emission profile in high-B_t condition

Measurement of the time-resolved neutron emission profile was conducted with an inward-shifted configuration R_{ax} of 3.60 m and B_t of 2.75 T. Here, the toroidal magnetic field direction was set to be clockwise when viewed from the top. The time evolution of an experiment performed for relatively high B_t and using N-NB is shown in Fig. 3. The yellow region indicates the region of interest for this study, i.e., the region in which the plasma becomes approximately stable. In these discharges, one NB was injected into deuterium plasma with T_{e0} of ~2 keV and n_{e_avg} of $1x10^{19}m^{-3}$. S_n had approximately the same value in both cases, at $1.5x10^{14}$ n/s. The time evolution of neutron counts without subtraction of the scattered signal is plotted at the bottom panel of Figs. 3 (a) and (c). Neutron emission profiles are almost unchanged during the quasi-steady state regime. Note that the maximum pulse counting rate, including both neutron and gamma-ray-induced pulses, was ~20,000 counts per second. Therefore, the pile-up rate of the pulse is low enough because the typical pulse width is 20 ns. Figures 3 (b) and (d) show the radial T_e and n_e profiles. Peaked profile of T_e and hollow profile of n_e are formed.

Line-integrated neutron profiles were deduced in these experiments (Fig. 4). The neutron counts were integrated within the region of interest, marked in yellow in Fig. 3.

Here, the scattered signal is evaluated using the outermost channel of the VNC1, e.g., R of 4.23 m. The red plot corresponds to the co-NB case, and the plot in blue corresponds to the counter-NB case. Here the neutron counts are normalized by the deposition power of a deuterium NB. As shown in Fig. 3 (a), in an experiment with relatively high B_t, the average of neutron counting rate in all the channels divided by the deuterium NB injection power was approximately 1,200 [cps/MW]. The neutron emission profiles in co- and counter-NB cases were slightly different. In the co-going case, the peak is located at R of ~3.75 m, which is slightly in the outer region compared with R_{ax}. On the other hand, the relatively flat top appears at R of 3.5~3.7 m in the counter-going case.

3.2 Measurement of neutron emission profile in middle-B_t condition

The neutron emission profile measurement was performed in a middle toroidal magnetic field with R_{ax} of 3.60 m and a strength, B_t, of 1.83 T, using deuterium N-NB, as shown in Fig. 5. Here, the direction of the toroidal magnetic field was counterclockwise when viewing from the top. During the discharge, hydrogen N-NB was additionally injected to sustain the plasma because the heating power of deuterium N-NB was not sufficient to support a plasma. T_{e0} was ~2 keV, and n_{e_avg} was $1.5 \times 10^{19} m^{-3}$. The time evolution of neutron counts without subtraction of the scattered signal is plotted at the

bottom panel of Fig. 5 (a) and (c). Neutron emission profiles are almost unchanged during the quasi-steady state regime. Note that the sightline located at R of 3.54 m was removed from the bottom panel of Figure 5 due to issues with the data acquisition system. Figures 5 (b) and (d) show the radial profile of T_e and n_e. The profile of T_e becomes gentle compared with the high-B_t case and the hollow profile of n_e is formed.

Line-integrated neutron profiles are shown in Fig. 6. In the case of middle B_t, the average of neutron counting rate in all the channels divided by the deuterium NB injection power was approximately 1,400 [cps/MW]. The normalized neutron counting rate was slightly higher than the neutron counting rate in the high B_t case because the plasma density was higher in the middle B_t case than in the high B_t case. Then, the relatively higher density induces improvement of NB deposition. Unlike in the high B_t case, the configurations of the line-integrated neutron profiles were different in co-NB and counter-NB cases. In the co-NB case, the peak was located at R of ~3.8 m, whereas in the counter-NB case, the peak was located at R ranging from ~3.4 to 3.6 m.

3.3 Measurement of neutron emission profile in low-B_t condition

The time evolution of a plasma discharge for the neutron emission profile measurement performed for a low toroidal magnetic field strength, B_t, of 0.6 T is shown

in Fig. 7. Here, the toroidal magnetic field direction was directed to be counterclockwise when viewed from the top. The hydrogen N-NB was also injected to sustain a plasma. T_{e0} was ~0.7 keV, and n_{e_avg} was $1.5 \times 10^{19} m^{-3}$. Due to electron temperature degradation, the neutron counts were considerably lower than the neutron counts for high or middle B_t cases. In a relatively low B_t case, T_{e0} was almost one-fourth of T_{e0} in high or middle B_t cases. According to the neutron flux monitor, S_n is approximately 2×10^{13} n/s. The time evolution of neutron counts without subtraction of the scattered signal is plotted at the bottom panel of Fig. 7 (a) and (c). Figures 7 (b) and (d) show the radial profile of T_e and n_e. The shape of T_e is similar to that of the middle-B_t case and a hollow profile of n_e is formed.

The unique profiles of the line-integrated neutron emission profiles were obtained in the low B_t case (Fig. 8). The average of neutron counting rate in all the channels divided by the injection power of the deuterium NB was approximately 200 [cps/MW]. Although S_n becomes almost one order smaller than S_n in high-B_t case, neutron counts reduce by one-sixth. This discrepancy might be due to the change of the neutron emission profile because S_n reflects global neutron emission. On the other hand, neutron counts measured by VNC reflect local neutron emission. It was reported that in the high-B_t experiment, the volume integrated neutron emission profile shows that neutrons are

mainly produced at normalized minor radius r/a of ~0.5 [31]. The discrepancy of the ratio of S_n and neutron counts in high-B_t and low-B_t suggests volume integrated neutron emission profile is vastly changed in the low-B_t case compared to in high-B_t case, as expected from Fig. 8. In the co-NB case, the peak position of the line-integrated neutron profile was R of ~ 4.0 m, whereas, in the counter-NB case, the peak of the line-integrated neutron emission profile was at R of 3.6 m. Furthermore, in the co- NB case, the steep gradient of the neutron emission profile was observed at R of ~4.1 m. It is found that the deviations of peak positions in the co-going and the counter-going cases became larger as B_t decreased.

4. Setup for Neutron Emission Calculation Based on Orbit-Following Models

A numerical simulation was performed using the DELTA5D code [32] to understand the measured line-integrated neutron emission profile in detail. The flowchart of the calculation is shown in Fig. 9. The equilibrium was reconstructed by the VMEC2000 code [33], using the radial profile of the electron temperature and the electron density measured by Thomson scattering diagnostics. Here, the ion temperature was assumed to be equivalent to the electron temperature. The configuration of the ion density profile was also assumed to be equivalent to the electron density, and the effective charge

was assumed to be Z_{eff}=3.0 from the previous evaluation of effective charge in a short pulse NB injection experiment performed in a similar plasma density region [34] with a constant radial profile. The birth profile of the beam ion was calculated using the HFREYA code based on the equilibrium, which is an aspect of the FIT3D code [35-37]. The guiding center orbit of beam ions from the birth positions of beam ion in the Boozer coordinates, including collisions with background plasma, is followed in the DELTA5D code for 1 s, which is longer than typical the neutron decay time due to slowing down and transport of beam ions in this density range ~500 ms [34]. The energy and spatial distributions of beam ions in the steady-state plasma are calculated by integrating every 0.5 ms the distribution function analyzed by DELTA5D. Five-dimensional distribution functions meant three dimensions of the spatial distribution, e.g., r/a, toroidal angle, and poloidal angle, plus two dimensions of velocity distribution, e.g., energy and pitch angle. The neutron emissivity in each spatial grid is calculated using the energy distribution of beam ions, deuteron density, and deuteron temperature. Here, we only consider a beam-thermal DD fusion reaction using the deuterium-deuterium cross-section using Ref. 38 because the beam-beam fusion rate is low because the relative velocity of beam ions injected by the same N-NB is small. The line-integrated neutron profile is calculated based on the neutron emission profile at the poloidal cross section, where the VNC1 is

installed. We randomly choose a thousand points on the detector surface and one thousand points on the upper end of the multichannel collimator using a random number generator to draw one thousand virtual line elements. The line-integrated neutron emission profile is calculated by the summation of the neutron emissivity along with the line elements with five-millimeter steps.

Figure 10 shows the typical collisionless beam ion orbit in Boozer coordinates calculated by the DELTA5D code. Figure 10 (a) shows the orbit of co-going ions whose energy and pitch angle are 180 keV and 38 degrees, respectively, for each B_t case. Here the pitch angle of 38 degrees is the typical pitch angle of beam ions deposited on the relatively outer region of plasma by a co-injection beam [39]. The start point of the guiding center orbit was set to be at a normalized minor radius, r/a, of 0.6 and a poloidal angle of 0 degrees (right-hand side of the figure). In the co-going case, the orbit shifts outward, as expected. At B_t of 2.75 T, the beam ion orbit almost traced the flux surface. The deviation of the orbit from the flux surface became more significant for B_t of 1.83 T. For B_t of 0.6 T, the orbit deviates significantly and stays only on the outer side of the plasma. Figure 10 (b) shows the orbit of a counter-going ion whose energy and pitch angle are 180 keV and 142 degrees, respectively, for each case of B_t. Here the pitch angle of 142 degrees is the typical pitch angle of beam ions deposited on the relatively outer region

of a plasma injected by a counter injection beam [39]. The starting point of the orbit was set to be at r/a of 0.6 and a poloidal angle of 180 degrees (left-hand side of the figure). In the counter-going case, the orbit shifted inward, as expected. The deviation of the orbit from the flux surface is more significant than that of the co-going case. The deviation from the flux surface became more extensive as the magnetic field strength decreased.

Figure 11 shows the time trace of beam ion energy in each B_t case calculating with DELTA5D code including the slowing down with background plasmas. Here, the beam ion energy is the averaged value of ten particles. Start points and initial pitch angles are the same as the collisionless orbit calculations shown in Fig. 10. The slowing down of beam ions becomes gentle as the increase of B_t in both cases because of relatively high electron temperature which induces a longer slowing down time of beam ions. In co-going transit cases the Spitzer slowing down time (τ_{se}) of B_t of 0.60 T, 1.83 T, 2.75 T at r/a of 0.6 are 61 ms, 307 ms, and 439 ms, respectively, whereas the velocity slowing down times evaluated by exponential fitting in Fig. 11 (a) at B_t of 0.60 T, 1.83 T, 2.75 T are 62 ms, 458 ms, and 559 ms, respectively. The ratio of the velocity slowing down time in DELTA5D calculation on τ_{se} in B_t of 0.60 T, 1.83 T, 2.75 T cases are 1.0, 1.5, and 1.3, respectively. The ratio at B_t of 0.6 T is unity because r/a position of the orbit is almost unchanged, as shown in Fig. 10 (a). The longer slowing down time in the orbit following

simulation compared to the Spitzer slowing down time in 1.83 T and 2.75 T cases is due to the orbital effect. This is because beam ion orbit passes the inner side of r/a, where the slowing down time is longer, compared to the initial r/a. The highest ratio is obtained at B_t of 1.83 T case because orbit reaches the most inner side of the plasma, as shown in Fig. 10 (a). In counter-going transit cases t_{se} of B_t of 0.60 T, 1.83 T, 2.75 T at r/a of 0.6 are 65 ms, 268 ms, and 356 ms, respectively, whereas the velocity slowing down times evaluated by exponential fitting in Fig. 11 (b) at B_t of 0.60 T, 1.83 T, 2.75 T are 80 ms, 296 ms, and 406 ms, respectively. The ratio of the velocity slowing down time in DELTA5D calculation on τ_{se} in B_t of 0.60 T, 1.83 T, 2.75 T cases are 1.2, 1.1, and 1.1, respectively. Unlike co-going transit cases, the ratio is almost unchanged as B_t because the shift of orbit from the birth r/a position is relatively small compared with the co-going cases. As shown in Fig. 10 (b) in counter-going transit cases, the orbit shifts to the inner side of r/a, where the slowing down time is longer, at the outward region, whereas the orbit shifts to the outer side of r/a, where the slowing down time is shorter, at the inward region. Relatively small deviation and pass through the inner and outer region of r/a compared with the start point may induce relatively small changes of slowing down time.

5. Neutron Emission Calculation Based on Orbit-Following Models

5.1 Calculation of line-integrated neutron emission profile in high-B_t condition

Figure 12 shows the two-dimensional neutron emissivity profile calculated using the distribution function of beam ions obtained by the DELTA5D code at the poloidal cross-section where the VNC1 is located. It is worth noting that S_n/P_{NB} [n/s/MW] obtained in the calculation is 8.4×10^{13} for co-going case and 7.5×10^{13} which are 1.2 and 0.8 times of experimentally obtained S_n/P_{NB}, respectively. In the co-NB case, the neutron emissivity had its peak in the equatorial plane. In the counter-NB case, the neutron emissivity has a hollow profile. Line-integrated neutron emission profiles were calculated considering the width and location of each sightline (Fig. 13). Here, the error bar on the x-axis indicates the poloidal Larmor radius evaluated using the injection energy of NB. The calculated neutron emission has a peak at R of ~3.7 m in the co-NB case, whereas in the counter-NB case, the peak is located at R of ~3.6 m, as observed in the experiment. The calculated profile is in approximate qualitative agreement with the experimental profile.

5.2 Calculation of line-integrated neutron emission profile in middle-B_t condition

Figure 14 shows the two-dimensional neutron emissivity profile calculated using the distribution function of beam ions obtained by the DELTA5D code at the poloidal cross-section, where the VNC1 is located. Note that S_n/P_{NB} [n/s/MW] obtained in the

calculation is 7.5×10^{13} for the co-going case and 7.2×10^{13} for counter-going which are 0.7 and 1.1 times of experimentally obtained S_n/P_{NB}, respectively. In the co-NB case, the neutron emissivity had its peak in the equatorial plane. In the counter-NB case, the neutron emissivity has a hollow profile. Line-integrated neutron emission profiles were calculated considering the width and the location of each sightline (Fig. 15). Here, the error bar on the x-axis indicates the poloidal Larmor radius evaluated using the injection energy of the NB. The calculated neutron emission has a peak at R of ~3.7 m in the co-NB case, whereas in the counter-NB case, the peak is located at R of ~3.6 m, as observed in the experiment. Although the signal in the inner side region of the co-NB case is higher in the experiment, the calculated profile is in approximate qualitative agreement with the experimental profile.

5.3 Calculation of line-integrated neutron emission profile in low-B_t condition

Figure 16 shows the two-dimensional neutron emissivity profile calculated using the distribution function of beam ions obtained by the DELTA5D code at the poloidal cross-section, where the VNC1 is located. It is worth noting that S_n/P_{NB} [n/s/MW] obtained in the calculation is 1.5×10^{13} for the co-going case and 5.0×10^{13} for the counter-going case which are 1.2 and 0.5 times of experimentally obtained S_n/P_{NB}, respectively.

In the co-NB case, the neutron emissivity had its peak in the equatorial plane but largely shifted to the outward of the torus. In the counter-NB case, the neutron emissivity has a relatively flat profile. Line-integrated neutron emission profiles were calculated considering the width and the location of each sightline (Fig. 17). Here, the error bar on the x-axis indicates the poloidal Larmor radius evaluated using the injection energy of the NB. Although the calculated neutron emission profile almost aligns with the calculated profile in the counter-NB case, in the co-NB case, the calculated profile has a narrower profile at the inboard side when compared with the experimental profile. The narrower nature of the calculated profile may be due to the orbit loss boundary or the effect of MHD instabilities. In the DELTA5D calculation, beam ion orbits are followed in Boozer coordinates. Therefore, the orbit loss boundary is the last closed flux surface. However, in an experiment, some of the beam ions crossing the last-closed flux surface can reenter the plasma region. In previous research, the reentering effect of beam ions in a relatively low field experiment was evaluated using the MORH code [40]. It was reported that the heating efficiency of the co-going beam became 1.8 times when the reentering effect was included in fairly low field conditions, e.g., B_t of 0.425 T. In contrast, there was barely a change in the heating efficiency of the counter-going beam [41, 42]. Besides, the number of reentering ions becomes significant when B_t is decreased for the co-going beam,

whereas the number of reentering ions is almost unchanged for the counter-going beam. The reentering effect is thought to be visible in a relatively low B_t configuration at the inward side for co-going beam ions, as predicted by previous research. Another possibility is the MHD instabilities. In the low-B_t case, the magnetic fluctuation amplitude normalized by B_t (b_{θ_tilda}/B_t) is substantially large 2.5×10^{-4} compared to in high-B_t 1.8×10^{-5} and middle-B_t 7×10^{-5} cases. Such MHD instabilities might enhance the transport of beam ions, which leads to the degradation of the neutron emission rate and change of neutron emission profile. The detailed analysis of the neutron emission profile in low-B_t case will be the future work.

5. Summary

Neutron emission profiles were measured using a VNC in the LHD plasma with tangential N-NB injected under various B_t conditions, where the neutron emission profiles are different due to the beam ion orbit and slowing-down time. The peak of the line-integrated neutron emission profile shifted significantly in the low B_t case relative to the high B_t case. Thus, the neutron emission profiles in the co-NB case and the counter-NB case move away from each other as B_t decreases. The experimentally obtained line-integrated neutron profile was compared with the calculated profile using the guiding

center orbit code DELTA5D with a VMEC2000 equilibrium. The orbit in Boozer coordinates showed that the deviation of the orbit from the flux surface becomes larger as B_t decreases, as expected. The slowing down time of energetic ions is longer compared with Spitzer slowing down time because of orbital effects. Although the calculated S_n/P_{NB} stays within a factor of two, the deviation of calculated S_n/P_{NB} from the experimental value varies from -50% to +20% and opposite directions for co- and counter going cases. One of the possible candidates for the deviation in the opposite direction might be Z_{eff}. The part of beam ions can hit the plasma-facing components which leads to the incidence of impurities. The hitting position on the plasma-facing components depends on the beam ion orbit decided by the magnetic field configuration and strength. The precise evaluation of Z_{eff} including the profile, which is our future work, will provide a better understanding of beam ion confinement in experiments and calculations. The peak of the neutron emissivity shifts inward in the co-NB case, whereas in the counter-NB case, the peak of the neutron emissivity shifts outward as B_t decreases. The line-integrated neutron profile obtained through calculation was compared with that obtained through the experiment. Although the calculated peak position aligned with the experimental peak position, the calculated profile was narrower at the inward side for the co-NB case for a relatively low B_t case. Possible explanations for this deviation are the reentering effect of beam ions and

the effect of MHD instabilities. The experimentally obtained neutron emission profile almost matches the profile calculated by guiding center orbit-following models in the middle to high B_t experiment.

Acknowledgments

This research was partly supported by NIFS Collaboration Research programs (KOAH037) and by the LHD project budget (ULHH034 and ULGG801). This work was also supported by JSPS KAKENHI Grant Number C19K03798, by the NINS program of Promoting Research by Networking among Institutions (Grant Number 01411702), by Japan/U.S. Cooperation in Fusion Research and Development.

References

[1] A. Fasoli et al., Nuclear Fusion **47** S264 (2007).

[2] W. W. Heidbrink and G. Sadlers, Nucl. Fusion **34** 535 (1994).

[3] D. L. Jassby et al., Phys. Fluids B **3** 2308 (1991).

[4] T. Nishitani et al., Nucl. Fusion **34** 1069 (1994).

[5] F. X. Söldner et al., Nucl. Fusion **30** 407 (1999).

[6] N. Javis, Plasma Phys. Contr. Fusion **36** 219 (1994).

[7] M. Isobe et al., Nucl. Fusion **46** S918 (2006).

[8] M. Osakabe et al., Nucl. Fusion **46** S911 (2006).

[9] A. Werner et al., Rev. Sci. Instrum. **72** 780 (2001).

[10] K. Ogawa et al., Nucl. Fusion **53** 053012 (2013).

[11] Y. Takeiri, IEEE Trans. Plasma Sci. **46** 2348 (2018).

[12] Y. Takeiri et al., IEEE Trans. Plasma Sci. **46** 1141 (2018).

[13] M. Osakabe et al., Fusion Sci. Technol. **72** 199 (2018).

[14] M. Isobe et al., Nucl. Fusion **58** 082004 (2018).

[15] K. Ogawa et al., Rev. Sci. Instrum. **89** 113509 (2018).

[16] K. Ogawa et al., Rev. Sci. Instrum. **85** 11E110 (2014).

[17] H. Kawase et al., IEEE Trans. Plasma Sci. **47** 462 (2019).

[18] S. Sangaroon et al., Rev. Sci. Instrum. **91** 083505 (2020).

[19] K. Ogawa et al., Plasma Fusion Res. **16** 1102023 (2021)

[20] K. Ogawa et al., Nucl. Fusion **58** 044001 (2018).

[21] K. Ogawa et al., Plasma Phys. Control. Fusion **60** 044005 (2018).

[22] K. Ogawa et al., Nucl. Fusion **59** 076017 (2019).

[23] H. Kawase et al., Plasma Fusion Res. **13** 3402122 (2018).

[24] K. Ogawa et al., Nucl. Fusion **60** 112011 (2020).

[25] S. Sangaroon et al., Plasma Fusion Res. **16** 1402039 (2021).

[26] M. Isobe et al., IEEE Trans. Plasma Sci. **46** 2050 (2018).

[27] M. Isobe et al., Rev. Sci. Instrum. **85** 11E114 (2014).

[28] D. Ito et al., Plasma Fusion Res. **16** 1405018 (2021).

[29] I. Yamada et al., Fusion Sci. Technol 58 **345** (2010).

[30] T. Akiyama et al., Fusion Sci. Technol 58 **345** (2010).

[31] H. Nuga et al., 16th Technical Meeting on Energetic Particles in Magnetic Confinement Systems – Theory of Plasma Instabilities 2019.

[32] D. A. Spong et al., Phys. Plasmas **18** 056109 (2011).

[33] S. P. Hirshman and O. J. Betancourt, J. Comput. Phys. **96** 99 (1991).

[34] H. Nuga et al., J. Plasma Phys **86** 815860306 (2020).

[35] S. Murakami et al., Trans. Fusion Technol. **27** 256 (1995).

[36] P. Vincenzi et al., Plasma Phys. Control Fusion **58** 124008 (2016).

[37] R. Seki et al., Plasma Fusion Res. **14** 3402126 (2019).

[38] S. Bosch and G. Hale, Nucl. Fusion **32** 611 (1992).

[39] K. Ogawa et al., Nucl. Fusion **52** 094013 (2012).

[40] R. Seki et al., Plasma Fusion Res. **3** 016 (2008).

[41] R. Seki et al., Nucl. Fusion **53** 063016 (2013).

[42] R. Seki et al., Plasma Fusion Res. **5** 027 (2010).

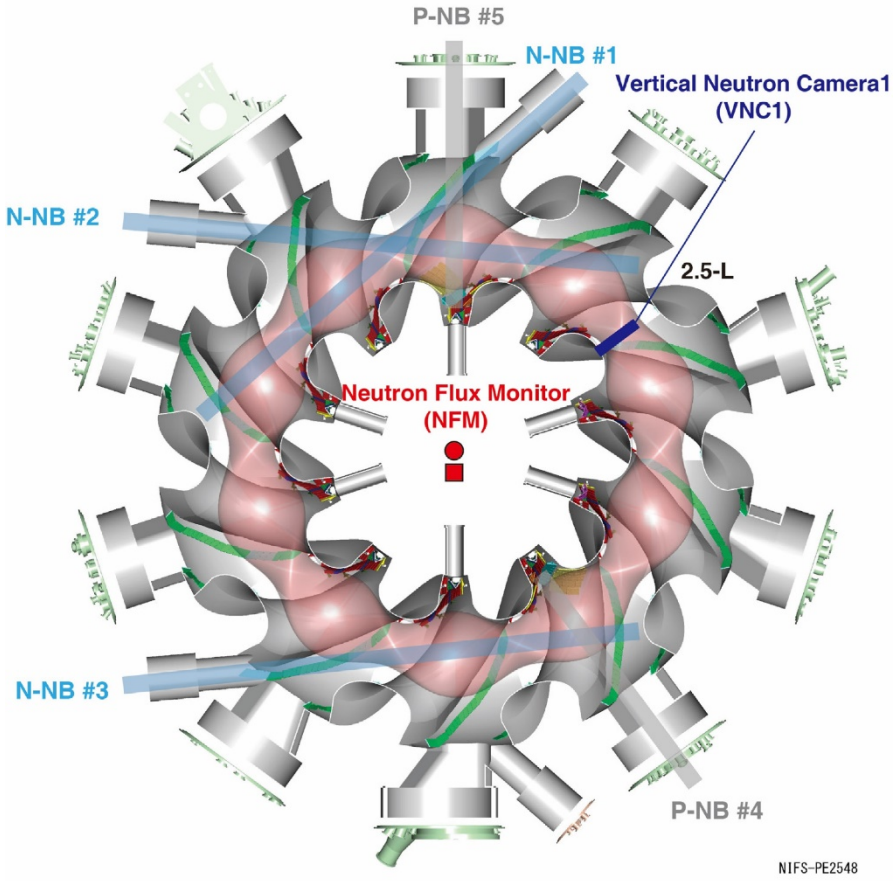

Fig.1 Top view of the LHD with the neutron flux monitor and vertical neutron camera 1.

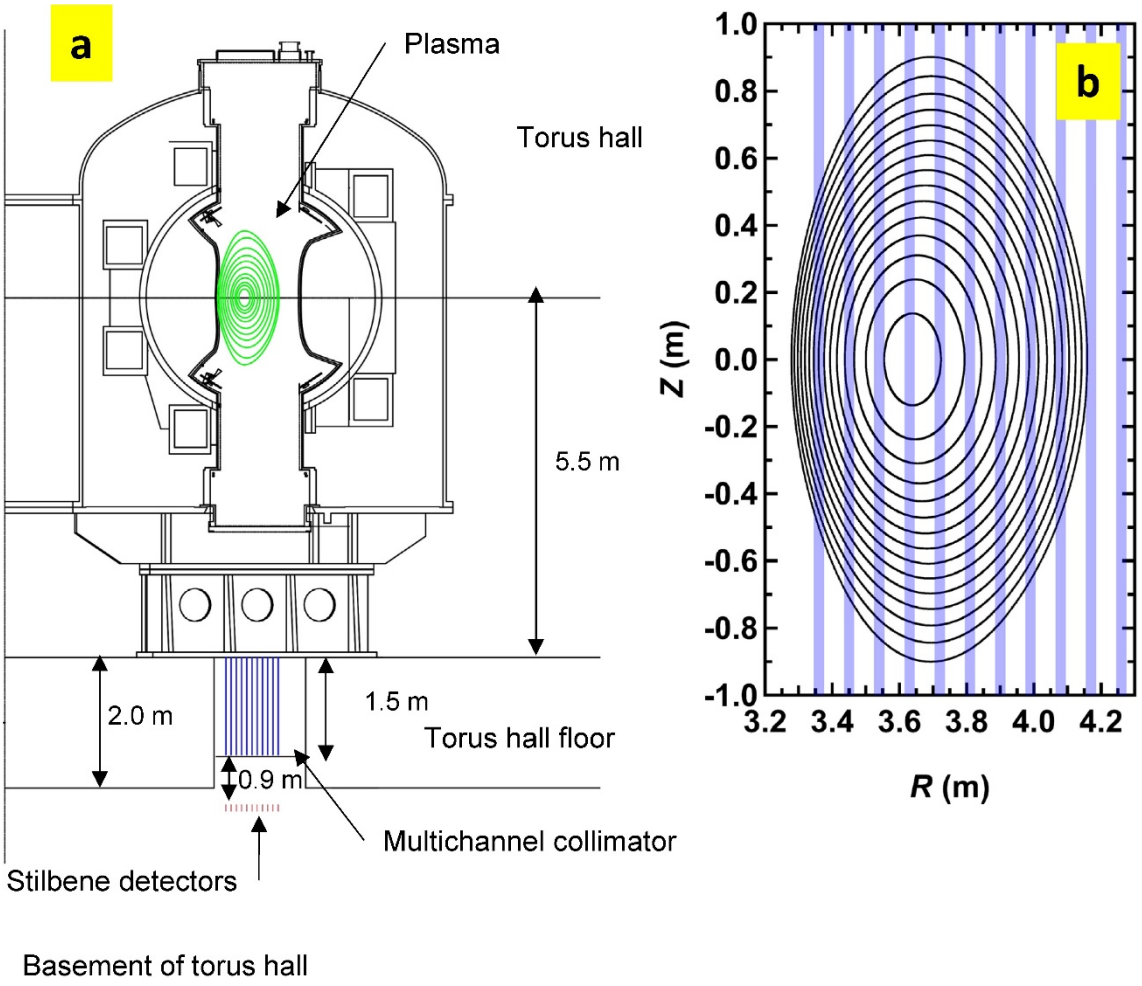

Fig. 2 (a) Schematic drawing of the vertical neutron camera. (b) Sightlines of VNC together with the poloidal cross-section of a plasma.

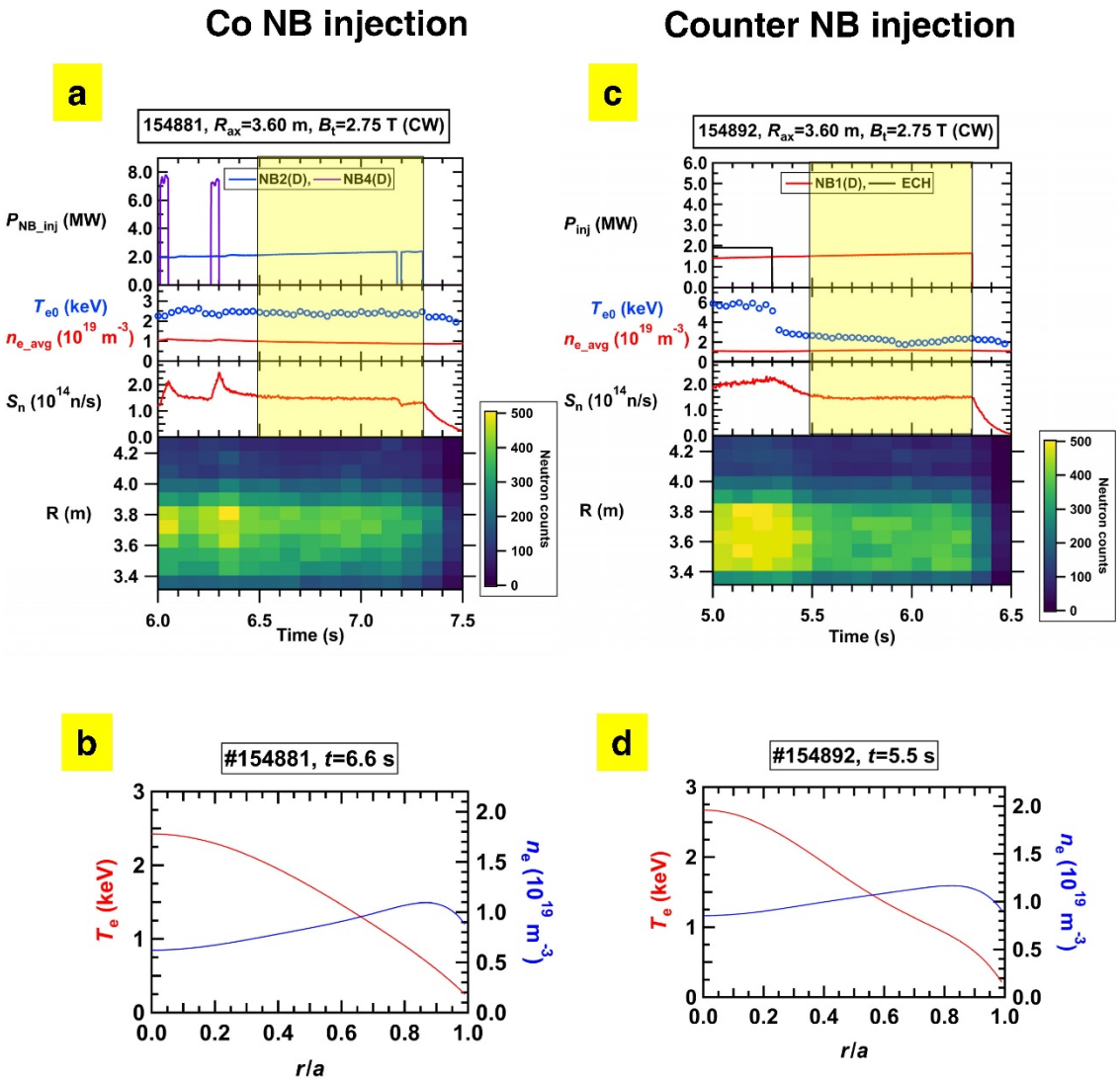

Fig. 3 Time evolutions of plasma discharges in high B_t conditions with (a) co-N-NB injection and (d) ctr.-N-NB injection. (b), (d) Radial profile of T_e and n_e measured by Thomson scattering diagnostics.

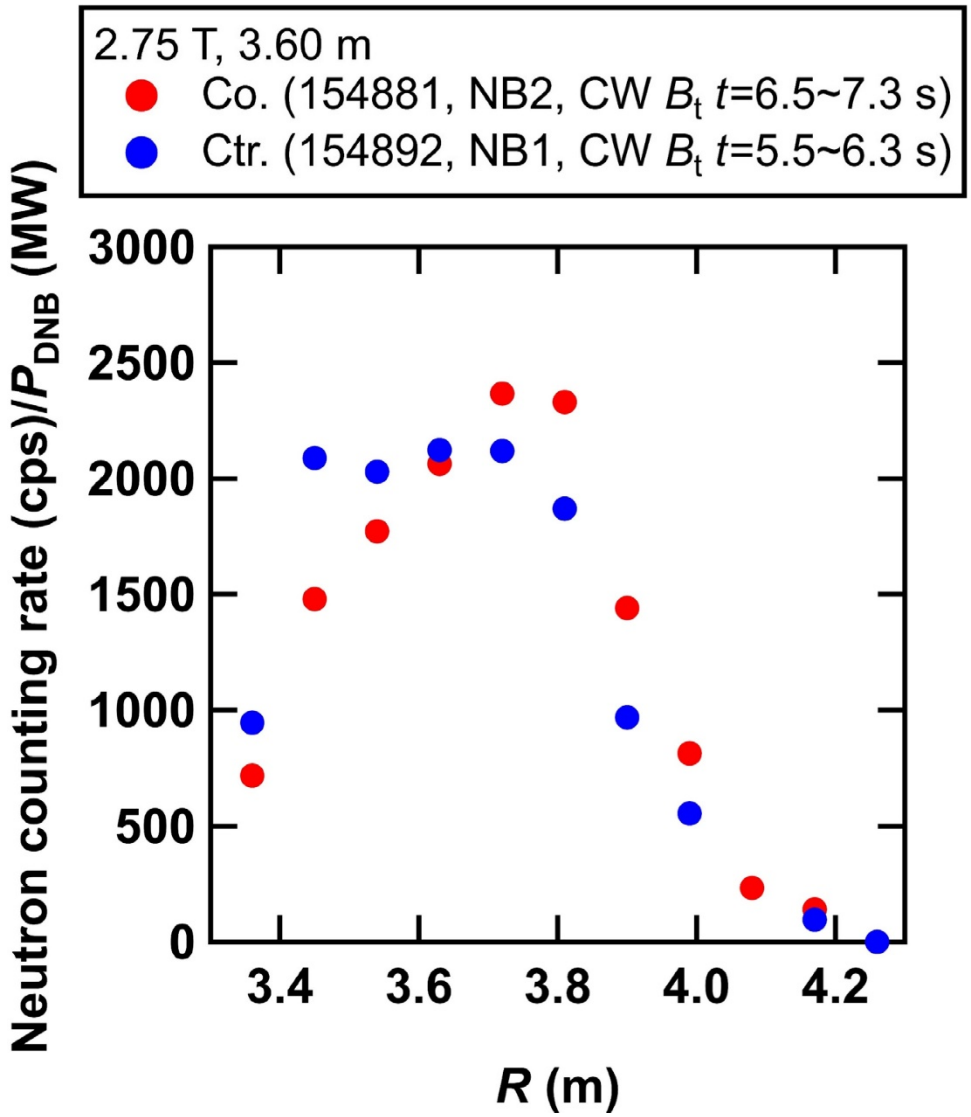

Fig. 4 Line-integrated neutron emission profiles obtained for a high B_t with N-NB injection.

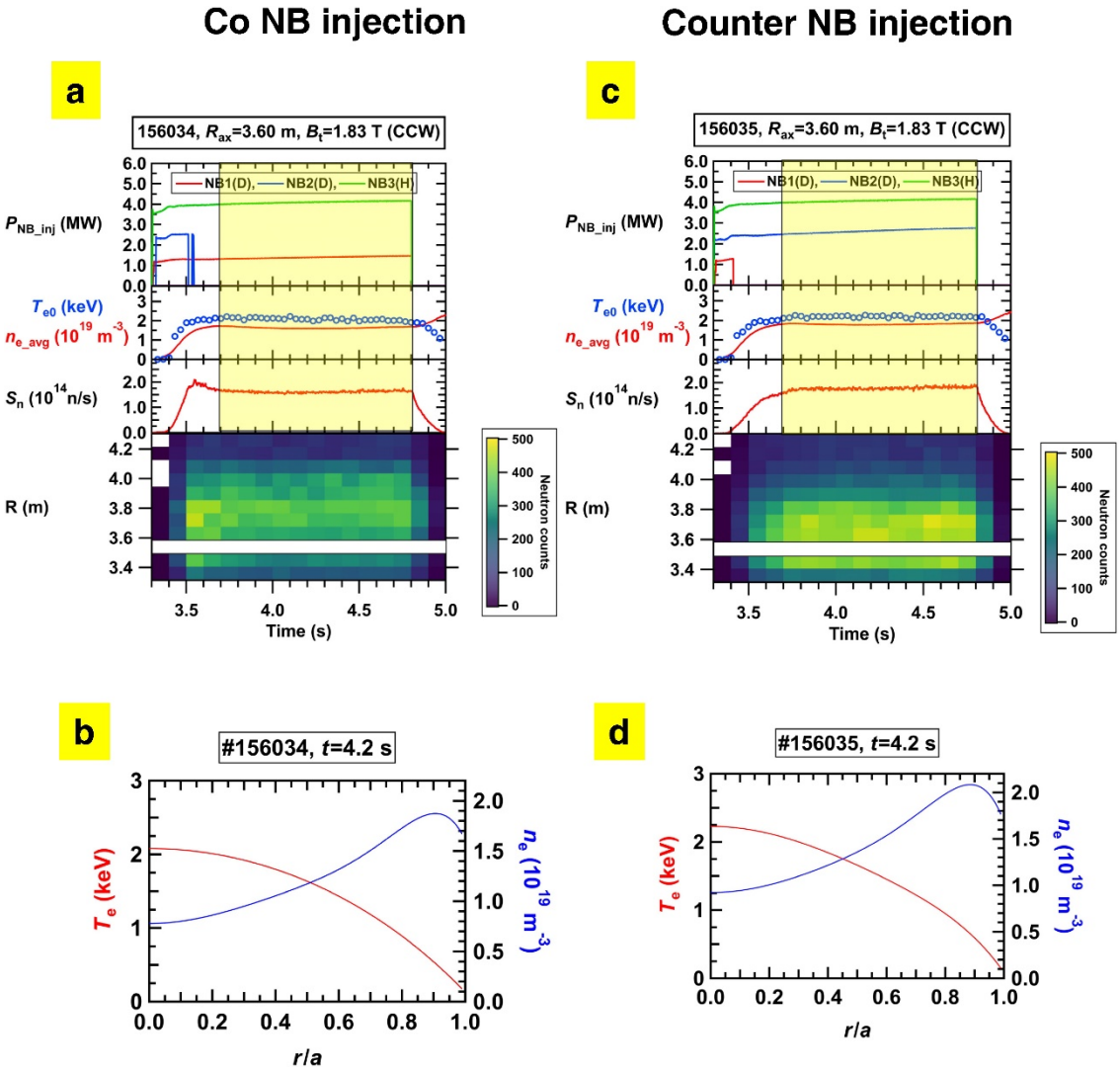

Fig. 5 Time evolutions of plasma discharges in middle B_t conditions with (a) co-N-NB injection and (c) ctr.-N-NB injection. (b), (d) Radial profile of T_e and n_e measured by Thomson scattering diagnostics.

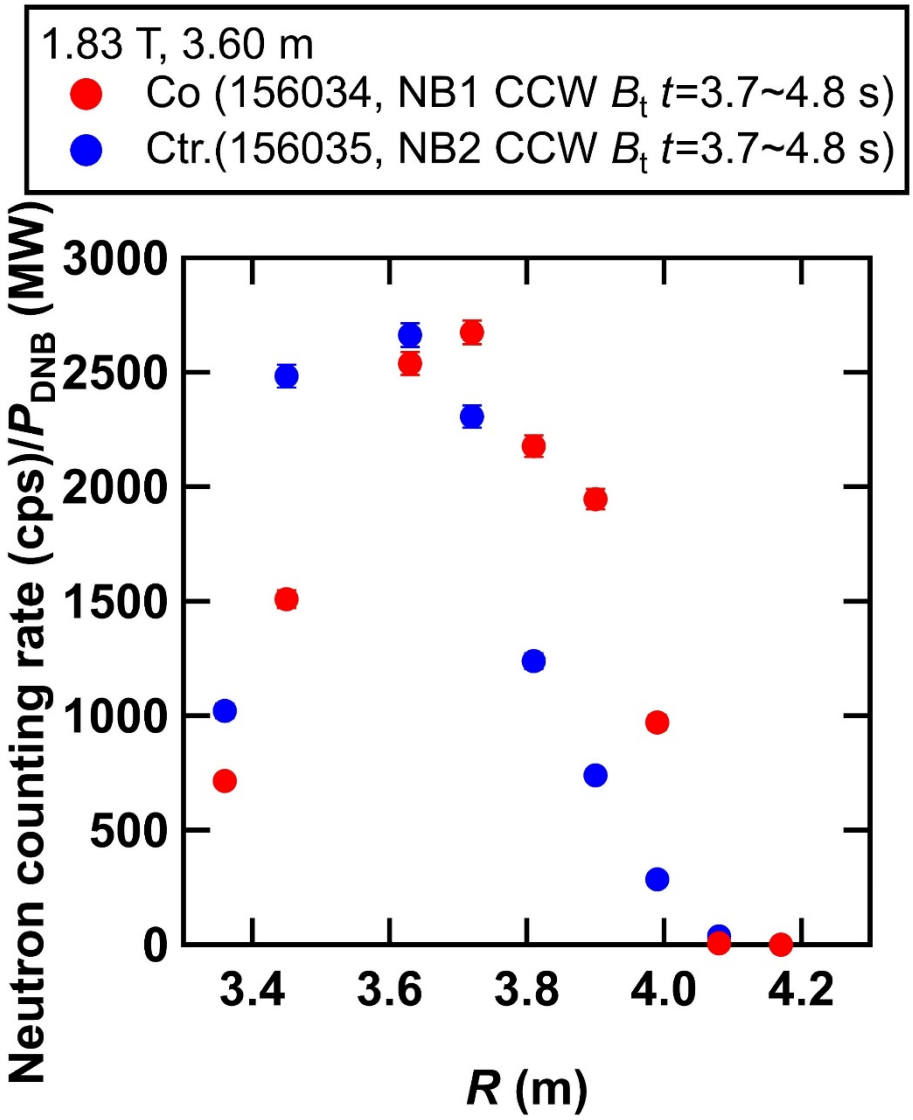

Fig. 6 Line-integrated neutron emission profiles obtained for a middle B_t with tangential N-NB injection

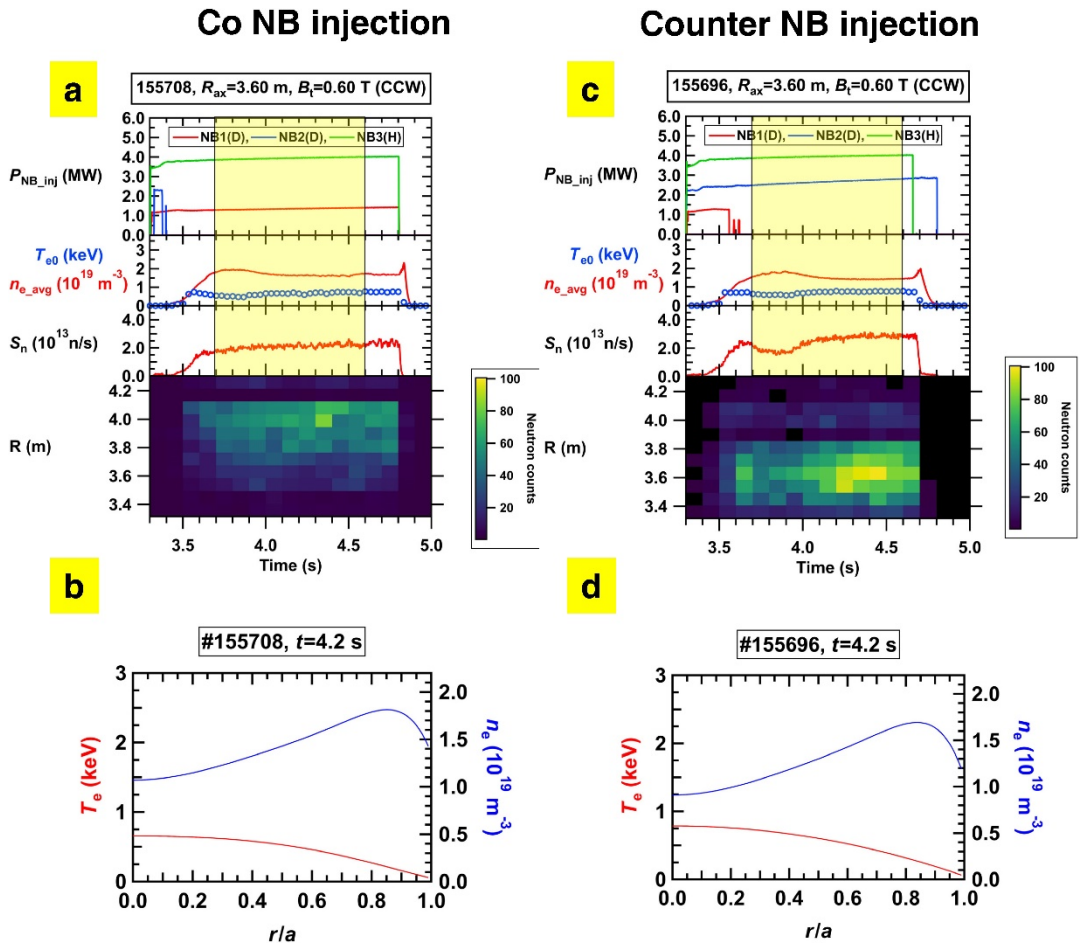

Fig. 7 Time evolutions of plasma discharges in low B_t conditions with (a) co-N-NB injection and (c) ctr.-N-NB injection. (b), (d) Radial profile of T_e and n_e measured by Thomson scattering diagnostics.

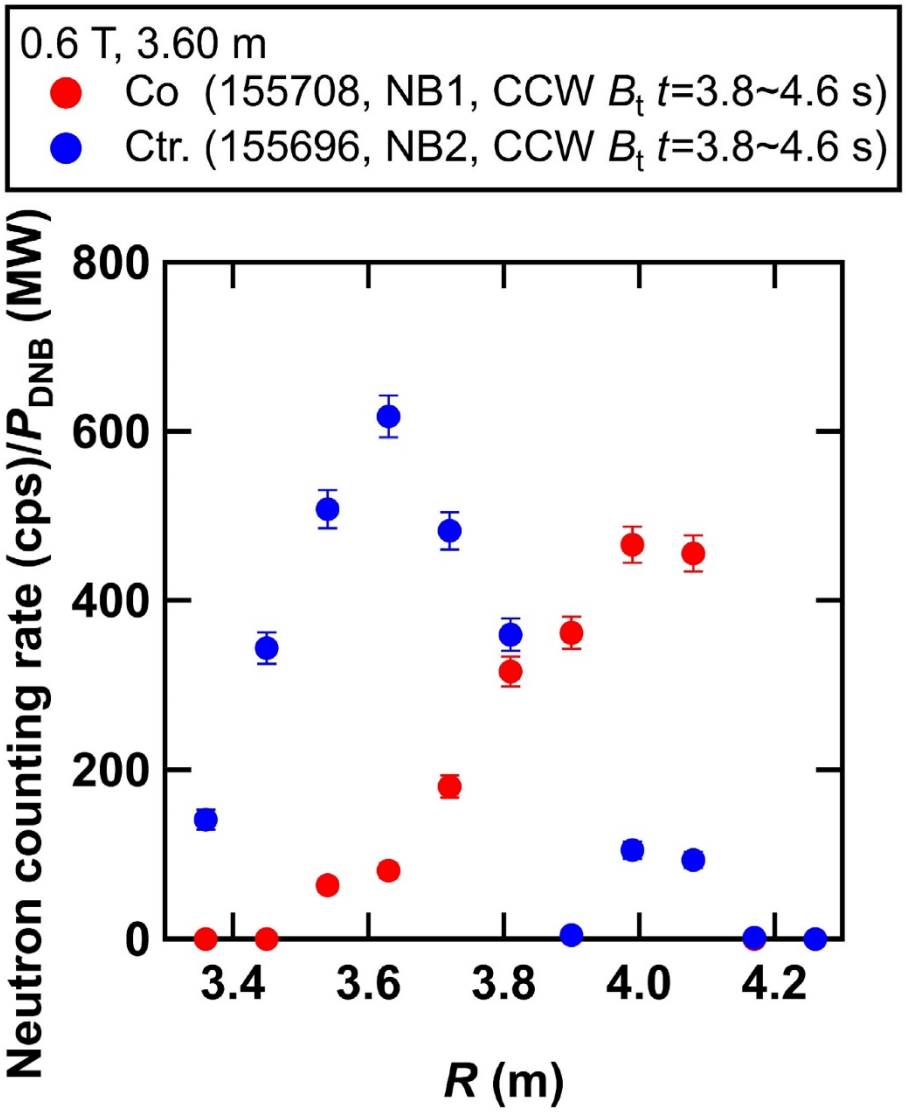

Fig. 8 Line-integrated neutron emission profiles obtained for a low B_t with tangential N-NB injection.

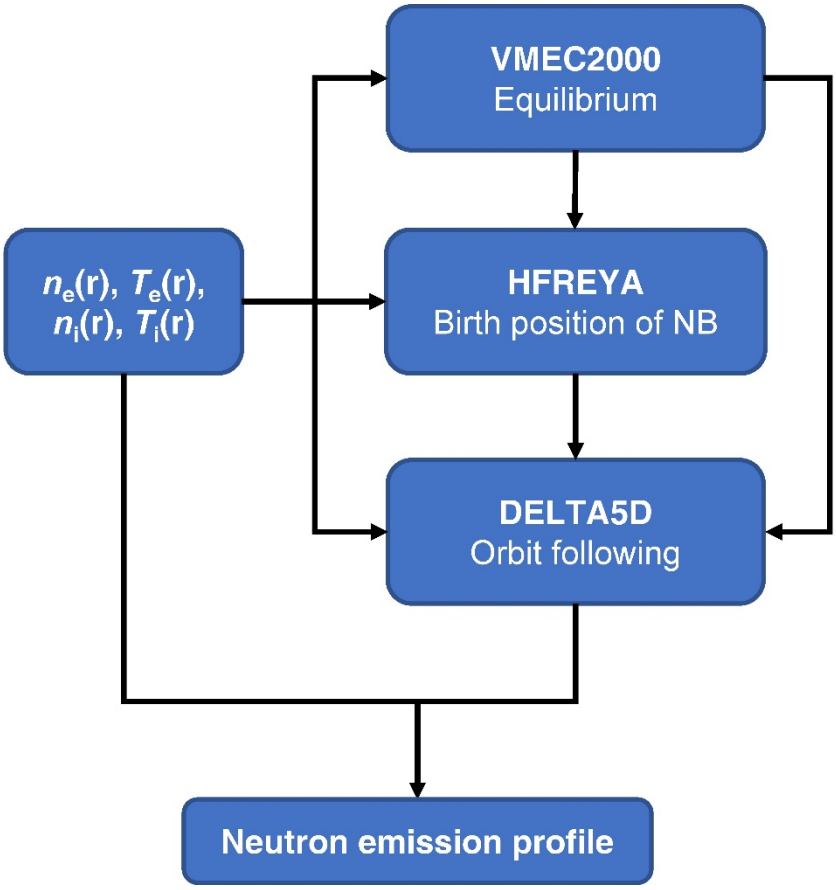

Fig.9 Flowchart of neutron emission profile calculation.

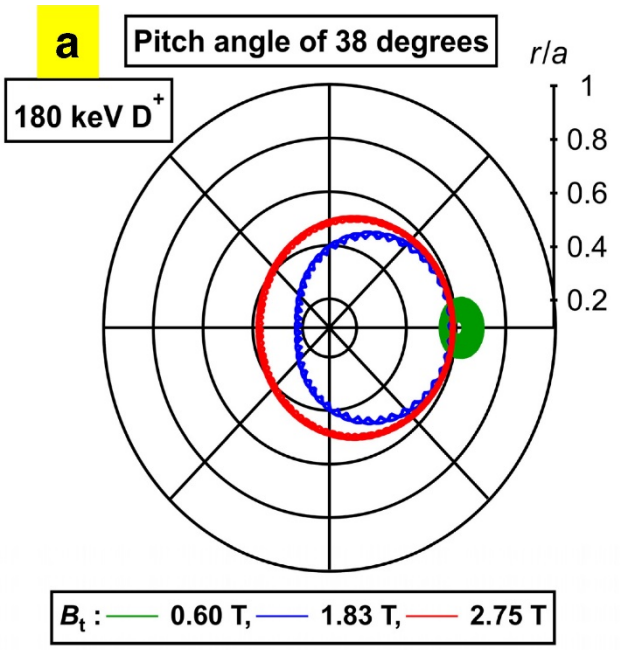

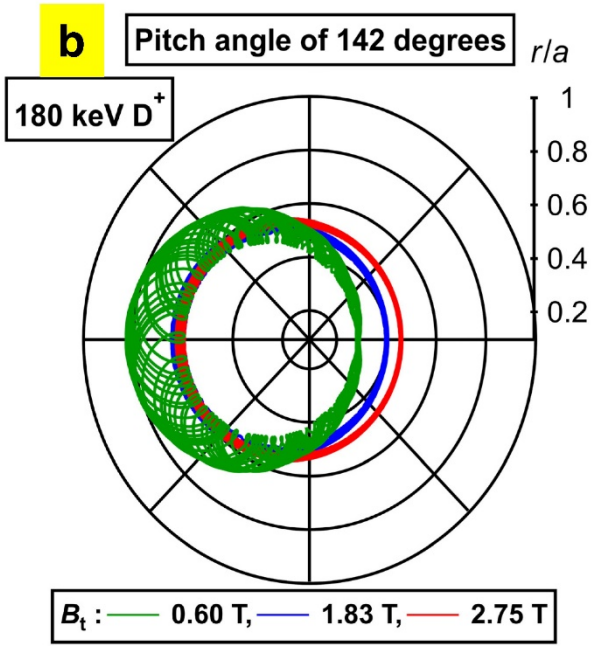

Fig. 10 Typical collisionless guiding center orbit in Boozer coordinates calculated with the DELTA5D code for (a) co-going transit beam ions, (b) counter-going transit beam ions.

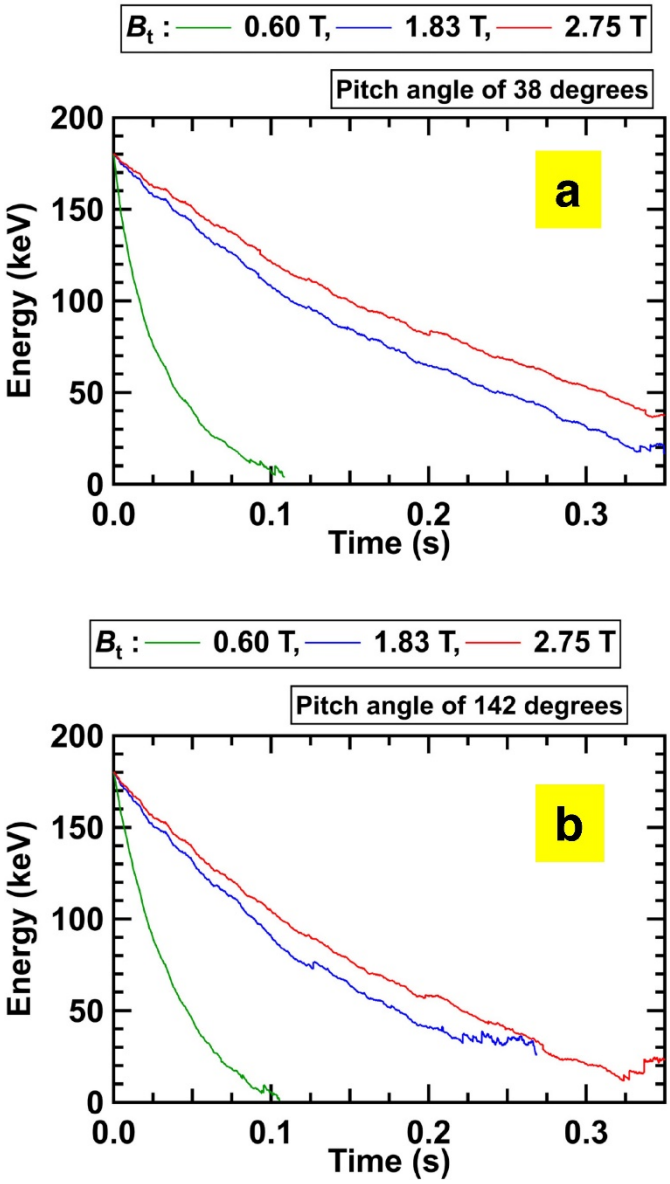

Fig. 11 Time evolution of beam ion energy calculated by DELTA5D code including the collision effect with background plasmas for (a) co-going transit beam ions, (b) counter-going transit beam ions.

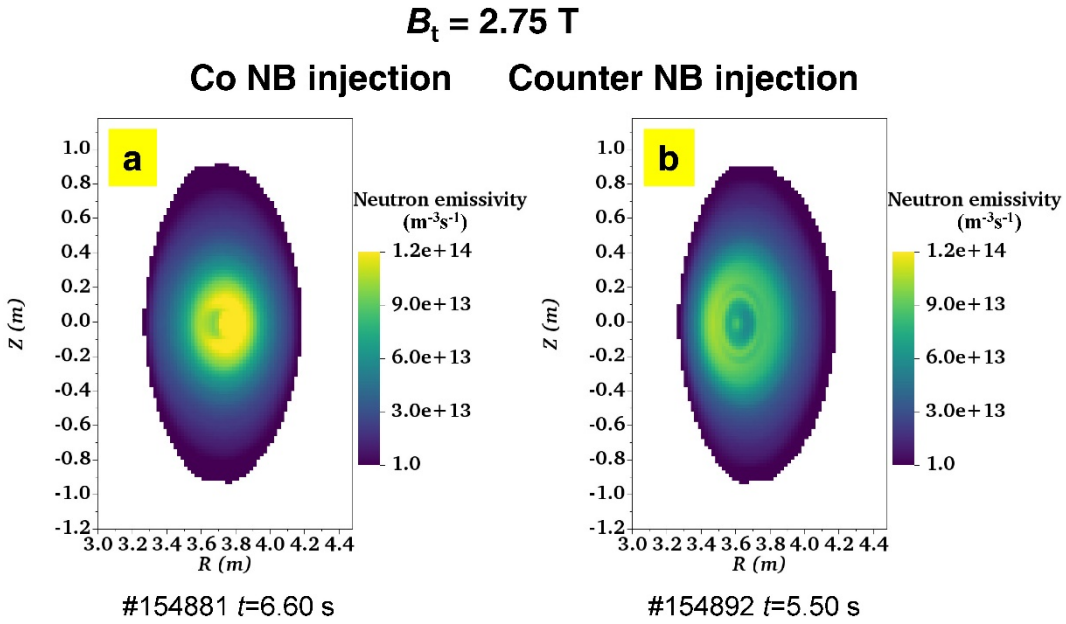

Fig. 12 Two-dimensional plot of neutron emissivity obtained from the numerical simulation in high B_t conditions with (a) co- and (b) counter N-NB injections.

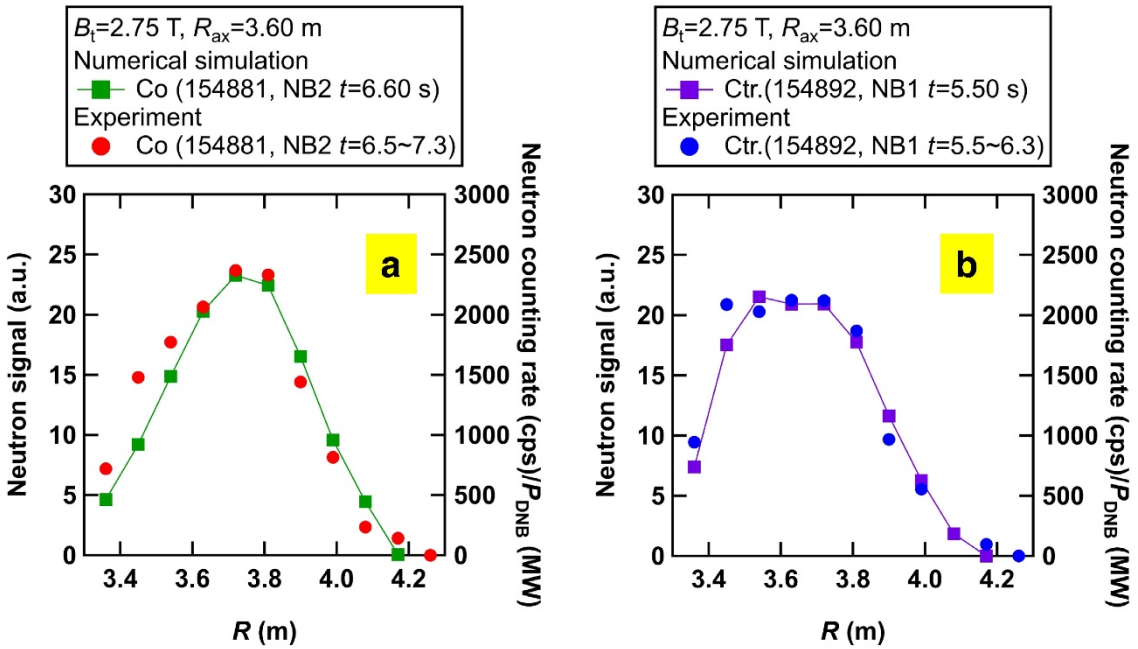

Fig. 13 Line-integrated neutron emission profiles calculated for a high B_t with (a) co-N-NB injection and (b) ctr.-N-NB injection.

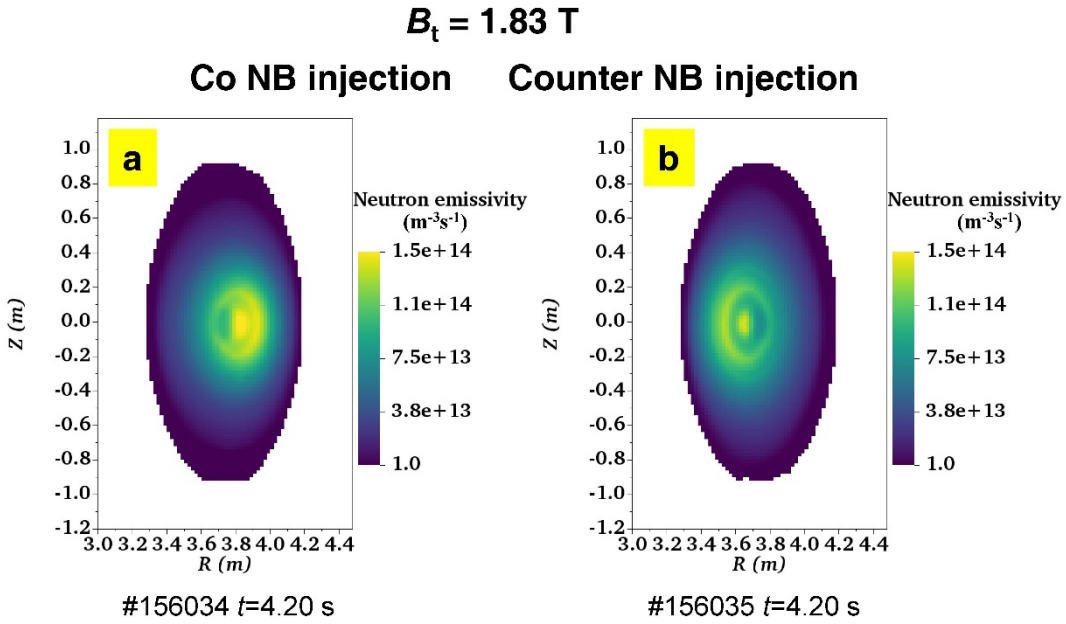

Fig. 14 Two-dimensional plot of neutron emissivity obtained from the numerical simulation in middle B_t conditions with (a) co- and (b) counter N-NB injections.

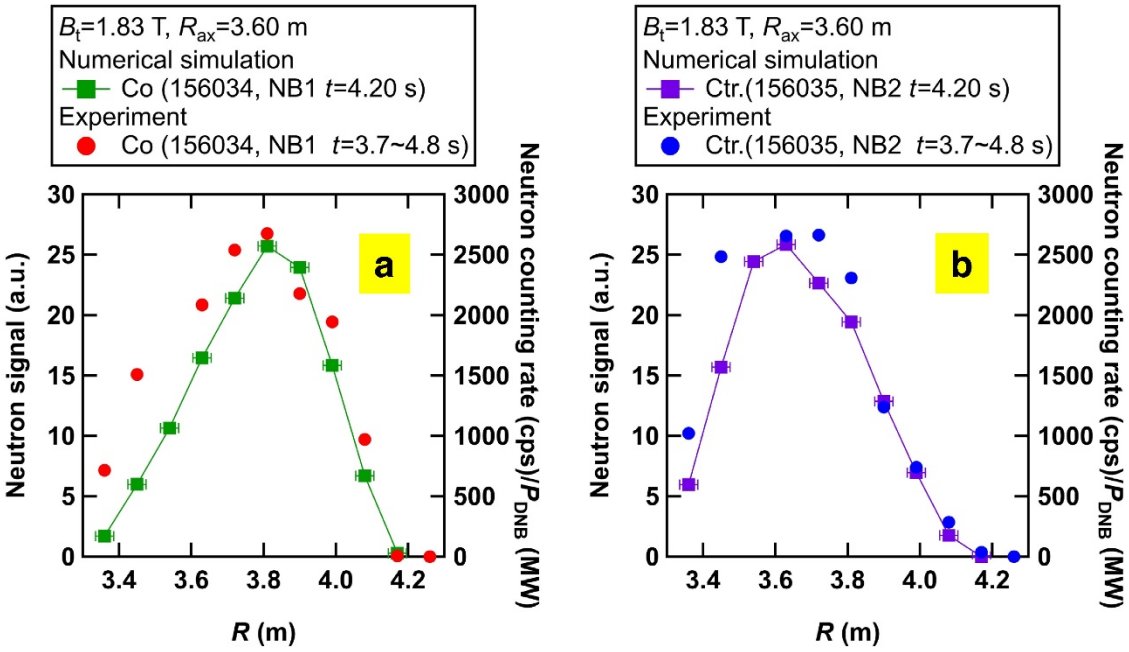

Fig. 15 Line-integrated neutron emission profiles calculated for a middle B_t with (a) co-N-NB injection and (b) ctr.-N-NB injection.

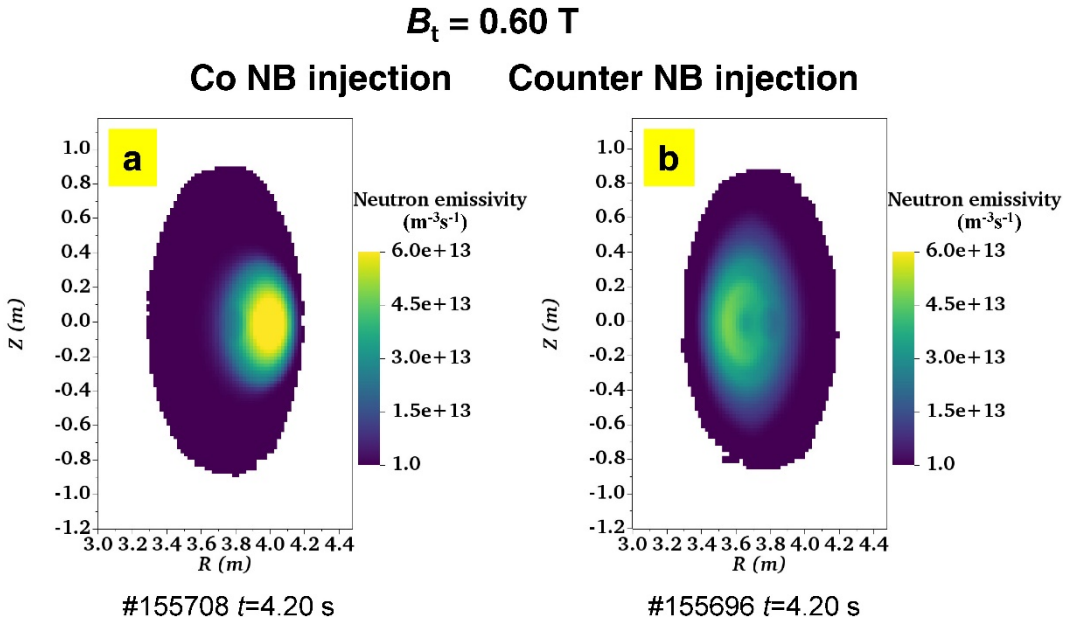

Fig. 16 Two-dimensional plot of neutron emissivity obtained from the numerical simulation in low B_t conditions with (a) co- and (b) counter N-NB injections.

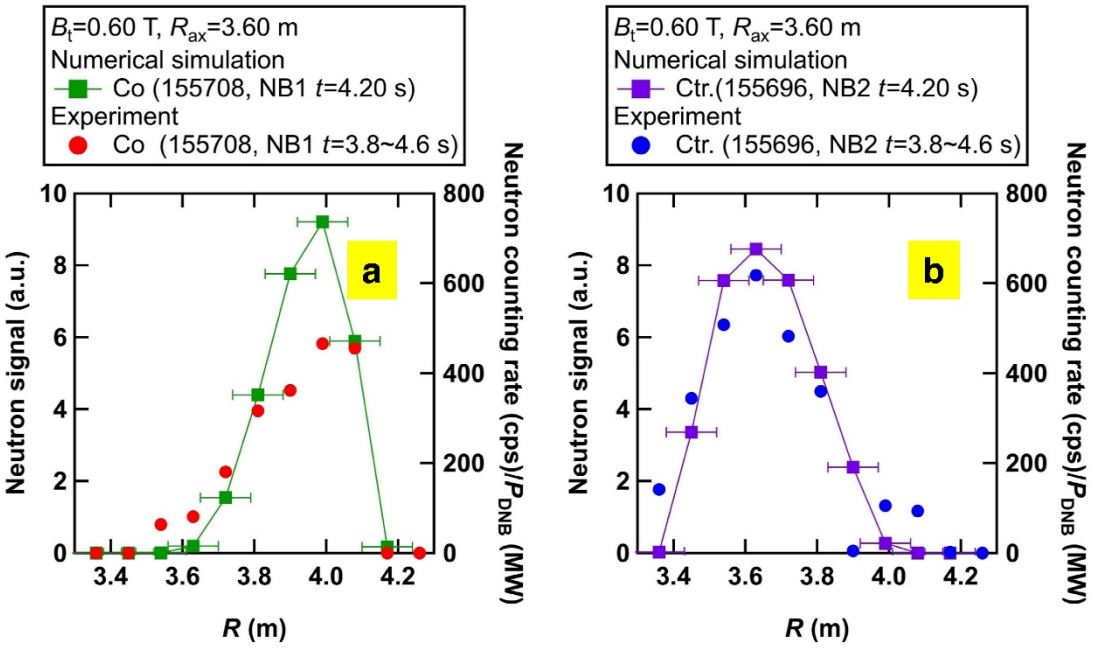

Fig. 17 Line-integrated neutron emission profiles calculated for a low B_t with (a) co-N-NB injection and (b) ctr.-N-NB injection.